Pacific Graphics 2019
C. Theobalt, J. Lee, and G. Wetzstein
(Guest Editors)

Volume 38 (2019), Number 7

Automatic modeling of cluttered multi-room floor plans from panoramic images

PAPER-1030

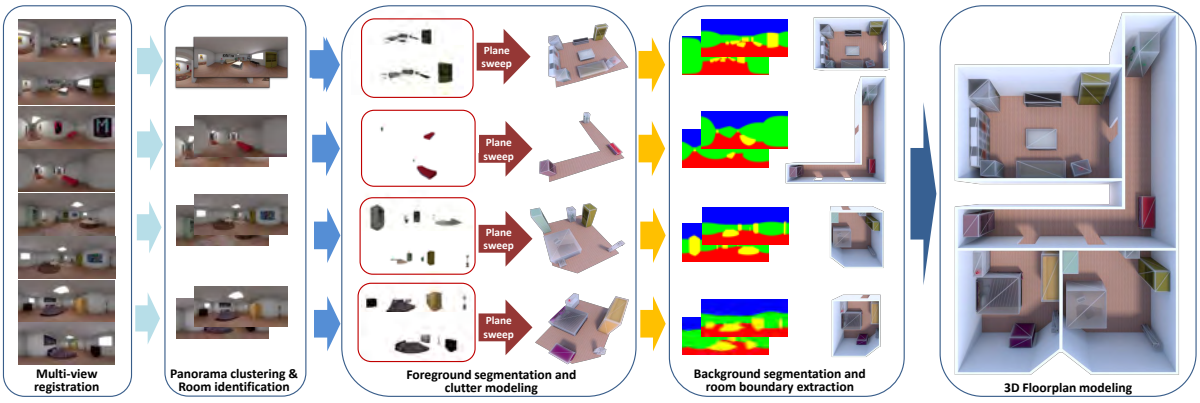

Figure 1: ***Overview.*** *Starting from a small set of overlapping panoramic images of a multi-room environment, we perform multi-view registration and extract, in parallel, the masks of interior objects visible in each image. Using mutual visibility and photoconsistency information, we group panoramas together with their masks into rooms sets, which are analyzed using a plane-sweeping approach to extract pose and size of interior objects. Finally, all the recovered information is exploited for the extraction of room boundaries and interconnections, leading to a structured indoor model in terms of rooms bounded by walls, ceiling, and floors and containing a set of objects described in terms of their bounding volumes.*

Abstract

We present a novel and light-weight approach to capture and reconstruct structured 3D models of multi-room floor plans. Starting from a small set of registered panoramic images, we generate automatically a 3D layout of the rooms and of all major objects inside. Such a 3D layout is directly suitable for use in a number of real-world applications, such as guidance, location, routing, or content creation for security. Our novel pipeline, which can handle cluttered scenes with complex geometry that are challenging to existing techniques, introduces several contributions to indoor reconstruction from purely visual data. In particular, we automatically partition panoramic images in a connectivity graph, according to the visual layout of the rooms, and exploit this graph to support object recovery and rooms boundaries extraction. Moreover, we introduce a plane-sweeping approach to jointly reason about the content of multiple images and solve the problem of object inference in a top-down 2D domain. Finally, we combine these methods in a fully automated pipeline creating structured 3D model of a multi-room floor plan and of the location and extent of clutter objects. The effectiveness and performance of our approach is evaluated on both synthetic and real models.

CCS Concepts

• ***Computing methodologies*** → *Computer graphics;* ***Shape inference; Reconstruction;***

1 Introduction

Creating high-level structured 3D models of indoor scenes from captured data is a fundamental task in many fields [BTS*17]. In this context, several applications, such as the generation or update of building information models (BIM) mostly focus on determining the architectural structure in terms of room walls, floors, and ceilings [MMJV*14, TCZ15]. For many others, such as guidance, security, evacuation planning, location awareness and routing, information on the interior clutter, in terms of 3D footprint of major indoor objects is also required [IYF15].

While a wide variety of solutions exists for capturing 3D information on indoor environments, from mobile laser scanners to a active depth sensors, the wide availability of mobile cameras, e.g., on smartphones, is making purely image-based methods very ap-

pealing. The visual capturing process is particularly fast, simple and cost-effective when exploiting emerging 360° cameras, since a good coverage of a complex environment generally requires very few shots, and such a panoramic coverage provides a visual representation readily usable in navigation applications [PGGS16].

Inferring indoor structure just from visual data is, however, not an easy task, due to the many ambiguities resulting from sparse coverage, occlusions, and lack of visual detail. The topic has thus been the focus of much research in the past decade. Current solutions, however, either require a fairly dense sampling generated by a large number of images in a texture-rich environment, or handle separately object and boundary reconstruction, often imposing very heavy constraints, requesting manual interventions, or addressing only single-room environments (see Sec. 2).

Our approach In this work, we propose a novel light-weight approach to compute, from a small set of registered panoramic images, a multi-room 3D layout in terms of room boundaries and 3D bounding volumes of all major objects (see Sec. 3). We use mutual visibility information and photoconsistency to create an interconnection graph between poses in order to split the image set in different room groups. We exploit this graph to simplify interior object identification and to support room identification and room boundaries extraction. The pose and size of the clutter objects in each room is recovered by starting from a per-image segmentation that identify the *masks* of indoor objects, and then using a *virtual plane sweeping* approach to jointly perform object inference in a top-down 2D domain using all the images associated to a room. The resulting 3D clutter model of all rooms, in terms of image mask, position, orientation and dimensions of each object, is then exploited to enhance image segmentation and geometric context reasoning for the room identification and room geometry extraction phases. As a result, the final model is partitioned into interconnected rooms bounded by walls, ceiling, and floors and containing a set of objects described in terms of their bounding volumes.

Contribution At the system level, we contribute a novel approach extending and combining in a non-trivial way several state-of-the-art solutions for indoor reconstruction from sparse panoramic images. We also introduce the following novel specific techniques:

- We introduce a photo-consistency approach to order and group the panoramic images in a connectivity graph. The core idea of our method is to detect rooms by clustering nodes in a fully connected graph, whose edges are weighted by the similarity among images under a specially crafted warping transformation. This grouping improves both object recognition and room structure identification, filtering undesired contributions from other images, such as, for example, images to far from the object or parts of other environments visible through open doors. Compared to previous approaches [PGP*18, CF14], which try to roughly infer walls position from the sparse input 3D points to estimate space partitioning, our approach provides more flexibility and robustness (see Sec. 7).
- We introduce a plane sweeping approach to solve the problem of object inference in a top-down 2D domain starting from single-image clues. To do this we define a specific *parameterization*, to transform in the same model space the contribution of different images, and a novel *loss function*, to evaluate object hypothesis. This approach allows us to by exploiting clues from different images, even if they do not fit on cuboids [ZSTX14]. Moreover, the approach is designed to work with an extremely limited number of images per object (e.g. 2-3), without involving the dense scene coverage required by other methods [IYF15, BFFFS14].
- We exploit the model of foreground clutter and the image grouping to enhance images segmentation and to complete rooms geometry extraction, i.e., to compute walls, floor and ceilings. This extra information improves current methods for indoor reconstruction from panoramic imagery (e.g., [CF14, YZ16, YJL*18, PGP*18]), which are mostly based on background segmentation via super-pixels. By exploiting clutter analysis in large-scale multi-room modeling, we produce a model which is more accurate and complete given the same number of panoramic images, as demonstrated by our results (Sec. 7).

2 Related Work

3D reconstruction and modeling of indoor scenes has attracted a lot of research in recent years. Resulting models usually are application-dependent, ranging from geometric to fully semantic reconstruction, and scale-dependent, from single rooms to large-scale scenes [IYF15]. In this work, we focus on pipelines from generating, from purely image data, structured geometric abstractions of multi-room environments with clutter [HDGN17, ZCC16].

From the capture point of view, many works require a fairly dense 3D point cloud of the environment. While in the past this was only possible with costly laser scanners, this approach is becoming more widespread due to the emergence of new sensors, including mobile RGB-D sensors. The methods, however still require a lot of post-processing to extract structured models from raw data [MMP16]. When it comes to the construction of a real 3D model (e.g., a mesh), existing methods typically produce a set of planar patches at a room scale [XAAH13], simple primitives for a part of a scene [GPMAL09], a dense mesh from a voxel grid [TCZ15] or a polygon soup without any structure or semantics [XF14]. For large scenes, current state-of-the-art methods solve room segmentation and reconstruction in a top-down 2D domain [TCZ15, MMP16]. A prominent example is the work of Ikehata et al. [IYF15], which propose a 3D modeling framework that reconstructs an indoor scene as a structured model exploiting panoramic *RGB-D* images.

In this work, we focus on purely image-based techniques, which are gaining popularity in several domains, since they are based on widely available and low-cost sensors. Even though, at least in certain situations, the accuracy of dense image-based methods has shown to be competitive with laser sensor systems at a fraction of the cost [SCD*06], the lack of explicit 3D information requires aiding reconstruction by imposing domain-specific constraints. For example, several authors exploit the heavily constraining *Manhattan World* assumption to reconstruct the 3D structure of moderately cluttered interiors e.g., [FCSS09, FMR11, TXLK11]) or the 3D footprint of interior objects (e.g., [LGHK10, HHF12]).

A number of authors have focused on joint estimation of room shape and object location in the single-view case, typically to infer room layouts from a single image. A classic approach, achieving good success with interiors containing large pieces

of furniture, is to analyze the scene by fitting 3D cuboid models [LGHK10, HHF10, HHF12]. These methods have been extended through Markov chain Monte Carlo (MCMC) sampling of part-based 3D object models [DBK*13] in order to achieve more accurate recovery of fine structures. Schwing et al. [SFPU13] used a branch-and-bound method to jointly infer 3D room layout and objects that are aligned with the dominant orientations, while Satkin et al. [SRLH14] proposed a top-down matching approach to align 3D models from a database with an image. The latter method employs multiple features to match 3D models to images, including pixel-wise object probability, estimated surface normals, and image edges. CNNs have also been used for the same purpose, as in the work by Su et al. [SQLG15], in which a CNN was trained for pose estimation using rendered models of 12 object categories from the PASCAL 3D dataset [XMS14], or in the work of Tulsiani et al. [TKCM16], which combine object localization and reconstruction from a single image using CNNs for detection, segmentation, and view estimation. These single-image methods are promising, but strictly limited to very small scenes, visible from a single point-of-view, and containing a limited number of object categories.

With the goal of minimizing user efforts and simplify modeling of entire rooms, recent state-of-the-art have extended single-image analysis to omnidirectional images. Some approaches exploit a super-pixel segmentation and an analysis of edges to recover room layout [YZ16] and depth estimation of the whole panoramic image [YJL*18]. These methods are limited to Manhattan-world environments and do not return a structured model. Recent data-driven approaches [ZCSH18, YWP*19] have also demonstrated success in recovering the 3D boundary of a single uncluttered room meeting the Manhattan World constraint, or to infer the whole context of a cluttered room containing a limited set of object categories [XSKT17, ZSTX14].

Multi-room environments typically require the joint analysis of images taken from multiple points of view. Bao et al. [BFFFS14], similarly to our work apply both single-view and multi-view reasoning to extend the number of recognized categories, but, in contrast to our work, focuses again on small scenes (i.e., room corners) and requires using a large number of pin-hole images (at least 10 images). The recent emergence of consumer spherical cameras promises to improve visual capture of indoor environment, since each image covers the complete environment around the viewer, simplifying geometric reasoning, and very few images are required for a large coverage, simplifying the capture process and the features tracking.

Cabral et al. [CF14] adopted stitched equirectangular images to improve indoor reconstruction provided by a dense multi-view pipeline [FCSS09]. As clutter and homogeneous zones in indoor scenes tend to leave large reconstruction holes for image-based methods, their method exploits the labeling of the panoramas to complete the multi-view reconstruction obtained from pin-hole images. However, such an approach required a considerable number of images and a dense point cloud, in addition to considerable efforts in terms of user interaction and processing time. Sharing the same simplified segmentation of Cabral et al. [CF14] (i.e., wall, ceiling and floor), Pintore et al. [PGP*18] recover the 3D layout of multi-room floorplans from a set of spherical images without involving externally calculated 3D data, by combining sparse multi-view features from images registration and single image analysis. Most panoramic imagery methods [YZ16, CF14, PGP*18, PPG*18] base image segmentation of on color homogeneity of indoor structures, a reasonable assumption for boundary structure but not for foreground objects.

In this work, we improve over prior techniques by automatically determining rooms, recovering clutter, and improving the accuracy of room shape recovering by effectively fusing multiple information sources coming out of room segmentation and clutter analysis.

3 Overview

Our pipeline, illustrated in Fig. 1, starts from a small set of omnidirectional images in the equirectangular projection. As prerequisites we assume that (a) input images are aligned to the gravity vector; (b) multi-view registration is possible; (c) target objects are visible from at least two point-of-view; (d) the bases of objects are below the camera horizon.

Constraint (a) is easily obtained on all modern mobile devices that have an IMU on board. Otherwise, vertical alignment can be obtained by rotating the global up vector so that the vertical edges are aligned with the vertical direction in the images. We thus consider vertical alignment to be a separate problem to be solved prior to the application pipeline, and we work only with oriented images. Constraint (b) and (c) require that images have at least some overlap, to ensure multi-view registration and detection of 3D features. In practice, this is obtained by 2-4 images per room. The last constraint is met by the vast majority of indoor objects, which are lying on the floor or attached to wall at low heights (e.g., furniture, sinks). The only objects that do not meet this constraint are objects hanging from the ceiling (such as lamps) or at the top of the walls (such as, for instance, some air conditioners). Such objects, however, are typically not necessary for most applications where it is important to determine room shape and walkable floor space.

Given just a set of images, we start by performing a multi-view registration to recover camera poses, multi-view 3D features and a bounding volume of the entire scene. In parallel, for each image, we classify image pixels into foreground (clutter) and background (wall, ceiling, and floor layout) exploiting a state-of-the-art approach for single panorama analysis [YJL*18]. As a result, we determine a *mask* for each panoramic image containing pixels from foreground. We then create an interconnection graph between poses, according to their mutual visibility and photoconsistency, in order to split the image set in different room groups (Sec. 4). We exploit this graph, together with poses, 3D features, and masks, to simplify object recovery (Sec. 5) and to support room boundary extraction (Sec. 6). Pose and size of the clutter objects (Sec. 5) are determined from the clutter segmentation and the room grouping using a *virtual plane sweeping* approach (Sec. 5.3), based on a specific parameterization (Sec. 5.1) and cost function (Sec.5.2). Clutter models are then used to enhance segmentation of the input images into floor, ceiling, and floor superpixels and to guide the extraction of room boundaries and interconnections (Sec. 6). As a result, we recover a structured 3D model of the floorplan comprehensive of clutter objects. We demonstrate the effectiveness and performance of our approach on different indoor scenes from public available datasets. (Sec. 7).

4 Partitioning of the panorama set

The room grouping aims to partition, without manual intervention or prior layout knowledge, the image set into rooms, in order to guide all subsequent analysis and geometric reasoning operations. Such a task requires the definition of a similarity measure between images, which should be high for images seeing taken in the same room, and low for all others.

Following this idea, our algorithm works in two steps. In the first step we build a graph connecting each pair of panoramic images that shares 3D points computed in the MVS registration phase, and weights each arc connecting two images with the likelihood that they were taken in the same room. In the second step we run a graph clustering algorithm based on *random walks* to obtain a connected component for each room.

One way of weighting the arcs could be using some image similarity criteria. However, in this setting is very likely that rooms of the same floor have the same type of furniture and the same type of color overall. Using a full-image similarity measure, moreover, would be hampered by the strong occlusions and distortions of indoor images, leading to possibly too strong differences between images taken from nearby viewpoints. A more local criterion may be to use the count of shared 3D features between panoramas. Let aside that in many cases the indoor scenario may contain few features. Even when there are many of them, it easily happens that panoramas taken nearby a door share a high number of features, no matter on which side of the door they were taken from. We thus use the fact that 3D points just to build the initial graph and not for arc weighting. We have experimentally found that initial graph construction is very robust to the number of shared features used as threshold for arc creation. All results presented here use a threshold of 10 shared features, which is low enough to avoid rejecting good candidates.

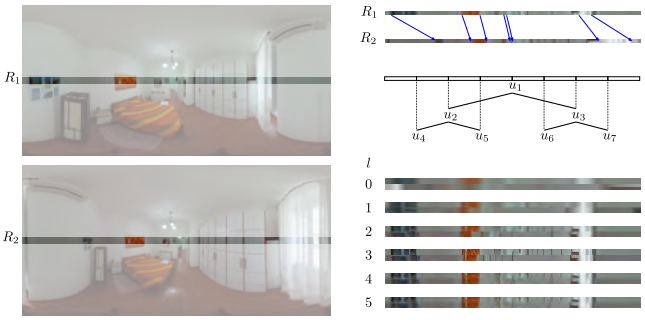

Figure 2: *Left: two images of the same room with the horizon stripes highlighted Right: top) correspondences between the two stripes R_1 and R_2; middle) hierarchical scheme for top-down computation of optimal warping; bottom) the first 5 levels of warping computation. Please note that the actual number of pixels for each level is $B2^l$. The stripes have been resized to the same length for the sake of comparison.*

The core idea of our method is, instead, that if we take two panorama images and manage to warp a reasonably, not-occluded portion of one image onto a matching portion of the other, then it's likely that they are images of the same room. In our case, we can, in particular, leverage the fact that all our panoramic images are acquired from the same height because it means that any warping will map pixels between the horizon rows of the two images, that is, the central horizontal rows (or close to them in case of approximate equal elevation, see Sec. 4.2). In other words, we are considering just an horizontal slice of each panorama taken at eye level, that typically means above chairs, tables and most other clutter. As it can be seen in Fig. 2.left discontinuities on furniture, corners, doors and windows are captured along with their topological relationship.

4.1 One-dimensional image warping

Let R_1 and R_2 be two rows of pixels. We obtain the warped version of R_1, $W(R_1)$, by defining the function $W : I\!R \rightarrow I\!R$ as the piece-wise linear interpolation of a series of k values $W(\frac{i}{k+1}) = u_i, 0 \leq u_i \leq 1, i = 1 \ldots k$. This warping is easily interpreted and implemented as the rendering of a texture mapped sequence of $k+1$ equally sized rectangles covering a row of pixels with the same width as R_1 and having $u_i, i = 1 \ldots k$ as texture coordinates. We proceed by iterating an optimization algorithm in a top-down fashion for' $k = 2^l$ $l = 0 \ldots l = log_2(\frac{n}{B})$, where n is the length of $R_{1|2}$ and B is the number of pixels at the minimal resolution. At each level l, the down-scaled version of $R_{[1,2]}$ are used, more precisely those with width equal to $B2^l$, and the error of a warping is computed as the average distance between the color of corresponding pixels, that is $E[|W(R_1) - R_2|]$. For $l = 0$ the warping is defined by a single variable/texture coordinate u_0, for $l = 1$ by 3 variables u_0, u_1, u_2, and so on. When the error minimization at level l is completed, the output values of the 2^l variables are passed to the next level $l+1$, and the remaining 2^{l+1} are initialized to random values.

4.2 Robust implementation

Although our approach is very straightforward, a robust implementation requires some more insights. First of all, any meaningful warping should have a bijective W, which means that variable u_i should be increasing, i.e., $u_i < u_{i+1}$. This is easily achieved by minimizing over a set of variables t_i that defines the u_i in a hierarchical way. In other terms $u_1 = t_1$, $u_2 = 0 * (1 - t_2) + u_1 * t_1$, $u_3 = u_1 * (1 - t_2) + 1 * t_2$ etc. Second, we use one more variable Δ as an offset to all the others, that is $W_\Delta(\frac{i}{k+1}) = \Delta + u_i$. This is done in order to more easily represent the rotational component between the two panoramas. Finally, we do not actually use a one-pixel-thick row of pixels. In order to account for little height differences between the shooting point of the panoramas and for small inaccuracies in vertical registration, we use a thicker row. On the other hand, please note that only pixels at the horizon are mapped to pixels at the horizon, that is, a linear warping is inaccurate for pixels off the central row. We found a working compromise by using 4 pixels thick rows. Please note that, for the sake of illustration, the stripes $R_{1|2}$ in Fig. 2 are much thicker (160 pixels).

4.3 Graph partitioning

We associate to each arc (i, j) the weight $w(i, j) = 1 - Err(R_1, R_2)$ where Err is the error corresponding to the optimal warping for a given pair. Given the weighted graph, we exploit a method based on random walks [HK01] to compute a partition of the images in groups, one group per room. The idea of the random walk methods is to interpret $w(i, j)$ as the probability that a traveling agent in i will move to node j. In this setting, letting agents walk in the graph will make the natural clusters emerge as the arcs internal to a cluster are traversed more often than the arcs connecting nodes of different clusters.

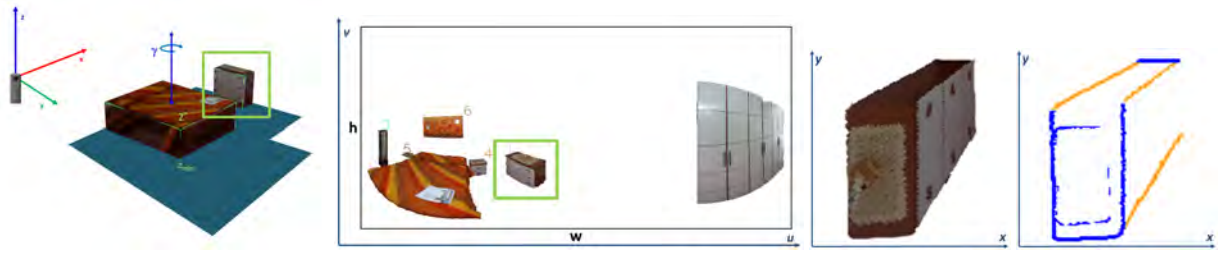

(a) *Object model* (b) *Image masks* (c) *rgb projection* (d) *Edges projection*

Figure 3: ***Foreground segmentation and projection.*** *We model each clutter object as a cuboid lying on the floor plan 3(a). Given objects contours/masks of an equirectangular image 3(b), we generate, for each z, a representative projection of each mask/object (i.e., hightlighted in green), both for rgb values 3(c) and edges 3(d).*

4.4 Parameter tuning and results

In order to verify that our method efficiently works without any manual intervention or per-dataset parameter tuning, we ran a series of tests in all datasets. In the table in Figure 4 the cells report the overall running times (in seconds) to complete the partitioning at several combination of stripes thickness T in $4, 8, 16$ (columns) and the optimization level L in $3, 4, 5$ (rows). The figure also shows the corresponding partition graph obtained by our algorithm, which is the same for all cases. This proves that changing the parameters has only effect on the running time but not in the final outcome, and that we can safely use the fastest configuration $T = 4, L = 3$ (top left cell of the table).

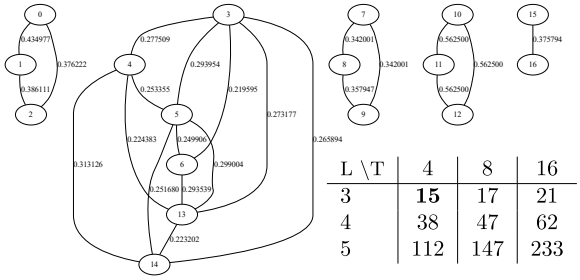

L \ T	4	8	16
3	**15**	17	21
4	38	47	62
5	112	147	233

Figure 4: ***Panorama partitioning for dataset R2****. Each rows shows a table of running time while varying thickness of the stripes and depth of the optimization tree, and the partition graph computed by the algorithm. Partitioning returns 5 rooms7.*

5 Recovery and modeling of clutter

We model each clutter object $O(z^*)$ as a cuboid whose *2D footprint* is an oriented rectangle $F(z^*)$. The bottom face of the cuboid lies on the floor plane (i.e, $z = z_{min}$) and the top face on the plane with $z = z^*$ (Fig. 3(a)). Assuming the floor plane is known, this cuboid is fully defined by 6 parameters, which are, respectively, 2D position, 2D size, orientation around z axis of $F(z^*)$, and height z^*.

Object identification is done per room through a geometric reasoning process that takes as input both per-image information and global information. At the image level, we segment the panorama into layout (background) and object (foreground) with the method of Yang et al. [YJL*18], which fuses the results of saliency and object detection algorithms to recover candidate object positions also when objects have unusual shapes or are partially visible. As a result, each panorama image is enriched with the pixel mask of candidate foreground objects. At the image group level, we exploit the output of our graph partitioning phase to apply all the reasoning phases only to images that are very likely taken in the same room, and therefore seeing (a subset) of the same objects. Multi-view registration is used to know the relative pose among images, as well as the position of a set of triangulated 3D features.

The cuboid representation of each model is inferred from all this information by introducing a *virtual plane sweeping* approach. We set the *virtual camera* (i.e., scene center) at the position of one the input cameras (i.e., the first one), looking the floorplan from the ceiling to the floor along z direction, also setting this pose as the center of the floorplan model (Fig. 3(a)). Object parameters are obtained by solving an optimization process. For this, we define a projective function (Sec. 5.1), to parameterize on z each image contribution, and a cost function $E(z)$ 5.2, to jointly evaluate the contribution of multiple images (Sec. 5.3). It should be noted that the object masks in individual images (e.g., Fig.3(b)) do not necessary describe a complete object shape but, as a result of automatic segmentation, only salient parts of it. Our goal, with the steps described below, is therefore to exploit different clues from different points of view to recover a consistent and complete model.

5.1 Parameterization

Let $P(x,y,z)$ be a point in object space and $R_k T_k$ the reference frame associated to the equirectangular image k (Fig. 3(b)). The correspondence between points and image coordinates (u,v) is established as follows:

$$u = \frac{\arctan(\frac{P'_y}{P'_x})}{2\pi} * w$$
$$v = \frac{\arctan(\frac{\sqrt{P'_x{}^2 + P'_y{}^2}}{P'_z})}{\pi} * h + \frac{h}{2} \quad (1)$$

where $P' = [R_k T_k] P$ are the local coordinates of the 3D point with respect to the k reference frame, w and h are respectively width and height of the image. Through this relationship, given a value of z, we can transform each image mask of an object into a representation on the XY plane (Fig. 3(b)) built from the corresponding image pixels. By matching these representations among several images for a given value of z, we aim to identify objects and determine their cuboid representation. Using this approach, object recovery can be cast as an optimization process of a matching cost function (Sec. 5.2), which is minimized through an efficient plane sweeping approach (Sec. 5.3).

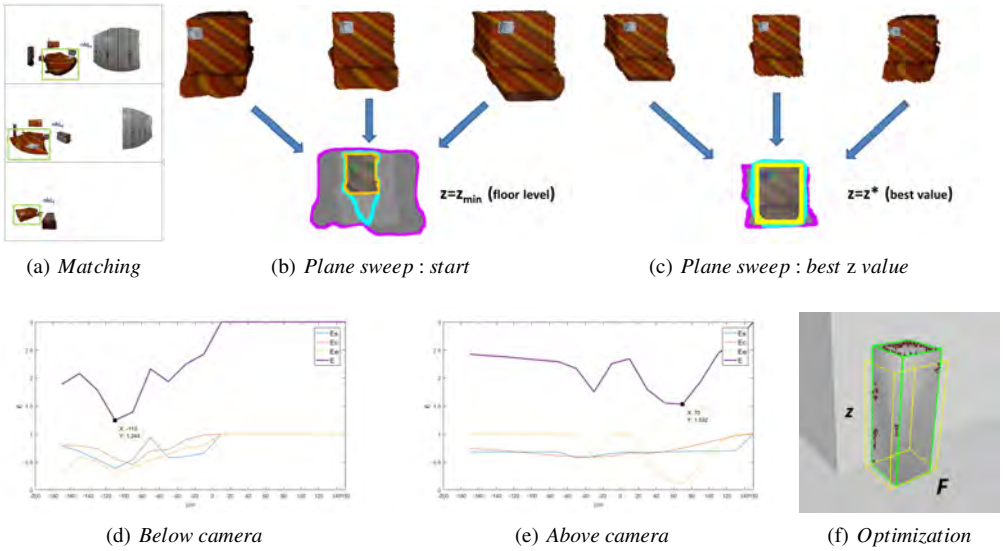

(a) *Matching* (b) *Plane sweep* : *start* (c) *Plane sweep* : *best* z *value*

(d) *Below camera* (e) *Above camera* (f) *Optimization*

Figure 5: ***Object modeling steps.*** *Fig. 5(a) shows the masks associated to object* obj_{id}*. Fig 5(b)shows the masks projection on the floor plane. Violet contour represents the union of the projections, Cyan contour their intersection, orange contour encloses points with best color consistency. Fig. 5(c) shows the projections of the masks when varying z, and in particular for the value* z^* *that minimizes the cost function. Yellow rectangle represents the recovered shape* $F(z^*)$*. Fig. 5(d) shows the cost function trend during plane sweeping for objects lower than the height of the virtual camera (e.g., same object-*Bed *of previous illustrations). Fig. 5(e) shows components trend for objects higher than the virtual camera (i.e.,* Cabinet *from* Apartment0*). Fig. 5(f) illustrates optimization step, where yellow boundary represents the initial* $O(z^*)$ *approximation and the green boundary the final fitting on the 3D sparse points.*

5.2 Cost function

We assume that at least $1 < m \leq n$ images contain a contour/mask of the same targeted object $O(F^*, z^*)$, where n is the number of images inside a group/room (Sec. 4).

We define the cost function $E(z)$:

$$E(z) = E_s(z) + E_c(z) + E_e(z) \tag{2}$$

where E_s, E_c, E_e denote different cost components, for a certain z, estimated by transforming and merging the m object masks and their contents. In particular, in addition to mask shape, the matching process uses image colors (Fig. 3(c)) as well as binary edge maps in (Fig. 3(d)) the mask area to determine a matching cost. In the case of edges, note that we remove vertical lines of the image (i.e., vertical structures in the world space), because, on the XY projection, they would only provide noisy information in terms of radial lines not consistent with the shape of the object (Fig. 3(d), orange edges).

Specifically, $E_s = 1 - IoU$ (*shape* component) measures the similarity among masks, and is a value that depends on the intersection over union ratio of the m projected masks (Fig. 5, cyan contour (intersection) violet contour (union)).

E_c, instead, measures color consistency, on the assumption that the same object viewed from different positions has the same color. To cope with lighting and shading variations, we compute this measure from the hue, computing standard deviation σ_i of k points lying inside the intersection, as $E_c = \frac{\sum_{i=0}^{k} \sigma_i}{k\ \sigma_{max}}$, normalized on a maximum std value (i.e., $\sigma_{max} = 4$).

E_e, the *edges* component, is meant to measure, instead, the consistence in shape, under the assumption that significant edges are consistent among views. In order to compute this component, we first determine the minimum area rectangle enclosing intersection points with $\sigma_{hue} \leq \sigma_{max}$ (enclosing orange contour of Fig. 5(b) and Fig. 5(c)), which is assumed to be the current 2D footprint $F(z_c)$ for the given z_c, so that the resulting 3D cuboid is $O(z_c)$. From the current 2D footprint $F(z_c)$ of $O(z_c)$, we compute E_e (*edges* component), as the 2D mean squared distance of the projected edges (Fig.3(d)) from the footprint $F(z_c)$, normalized to a max range (i.e., $50cm$).

In other words E_s evaluates how much the projected shapes of the same object coincide and fall on the same portion of space, E_c evaluates the consistency of the color, while E_e the consistency of the estimated shape edges with the color gradient. We exploit such cost function $E(z)$ in the optimization described in Sec.5.3.

5.3 Object recovery through multi-view optimization

At the beginning of the optimization, we determine the potential objects by analyzing mask overlaps and the behavior of the energy function. We initialize the system by determining which masks m are related to the same object obj_{id} (Fig. 5(a)). We set constant $z = z_{min}$ (i.e., z value for the floor with respect to the scene center) and we compare, in world projected space, each object mask vs. all the masks in the other images. If one or more intersection exist (Fig. 5(b)), we assign the same label obj_{id} on different images to the intersecting projected masks, choosing, in case of multiple intersections, the one with the minimum value of $E(z_{min})$. As a result of this initialization we obtain a list of target objects and, for each one, a list of m image masks related to that object.

Once a matching is established we perform, for each object, a plane sweeping, in the z direction, searching for the $z^* \in [z_{min} \dots z_{max}]$ which minimize $E(z)$, where $z = 0$ is the height of the virtual camera. Fig. 5(b) shows the projection of 3 masks for the initial z value (e.g., $z = z_{min}$), while Fig. 5(c) shows the projection

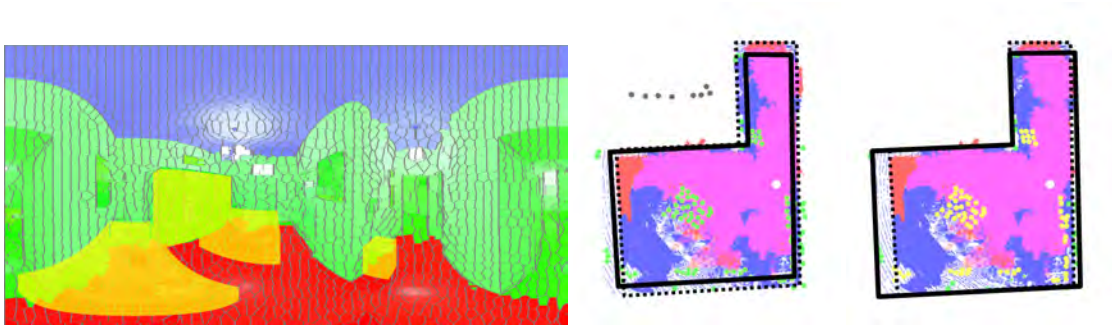

(a) *Segmentation with clutter* (b) *Fitting no clutter* (c) *Fitting with clutter*

Figure 6: ***Floorplan modeling.*** *Fig. 6(a) shows an alpha comparison between background labeling without considering clutter 3D models (blue (ceiling), red (floor) and green (wall)) and the labeling with projected clutter (yellow). Under the yellow labelled part is visible a glimpse of the segmentation without clutter [CF14] . Fig. 6(b) shows the room shape fitting without considering clutter. The initial shape estimated on ceiling-floor facets (dashed line) is shaped indistinctly on both anchor points of the wall and of the clutter. Grey dots instead represent points seen through a door but actually belonging to another room. Such points are filtered through the grouping information. Fig. 6(c) shows instead the fitting considering clutter information, which results in a more accurate reconstruction.*

in the proximity of the minimum of $E(z)$ (i.e., *Bed* from *Apartment0* dataset, see results 7). Figures 5(d) and 5(e) illustrate the trend of E components during plane sweeping. Fig. 5(d) shows the typical trend for objects below the virtual camera, i.e. objects whose upper part is visible from the camera. In this case the main contribution to the finding of minimum is given almost exclusively by *shape* and *color* components. Since objects under the camera can be identified a priori by the position of their masks in the images (e.g., all masks below the horizon), plane sweep is stopped in advance for $z = 0$.

Fig. 5(e), instead, shows the components trend for objects higher than the model center (i.e., *Cabinet* from *Apartment0*). Unlike the previous case, the components of shape and color are not very influential for the estimation of the height of the object, as the upper surface of it is not visible. Instead, the identification of the edges becomes discriminating, as evidenced by the trend in the graph.

As a result of plane sweeping we obtain a first approximation of the object $O(z^*)$ varying only z.

We exploit $O(z^*)$ to refine the model by varying all the 6 parameters $(\bar{F}, z)$, varying them independently but constrained around $O(z^*)$ (Fig. 5(f), yellow shape. Numerical details at Sec.7). we formalize the optimization problem as (Eq. 3):

$$O^*(\bar{F}, z) \equiv \underset{\bar{F},z}{arg\ min}\ [E_c(\bar{F}, z) + E_e(\bar{F}, z) + E_f(\bar{F}, z)] \qquad (3)$$

which can be solved with Levenberg-Marquardt iterations.

Differently by cost function in eq.2, in this case we do not compute E_s (e.g., footprint is already defined by $\bar{F}$, as well as E_c and E_e are computed directly on the candidate footprint $\bar{F}$. Additionally we introduce the E_f component, which is the mean squared distance of the 3D features (recovered from the multi-view registration) from the cuboid faces (Fig. 5(f), green shape). We iterate object recovery for each object and for each room until we populate the scene with all the 3D clutter models. We then exploit 3D clutter data to complete and enhance the reconstruction of the whole floor plan with room walls and ceilings (Sec. 6).

6 Recovery and modeling of the structural 3D floor plan

To recover walls, ceiling, and floor, we combine and extend state-of-the-art approaches for large and complex indoor scenes, exploiting the results from graph partitioning and clutter modeling.

As discussed in Sec. 2, current methods generally exploit a simplified image segmentation into ceiling, floor and wall super-pixels (e.g., [CF14, PGP*18]), where basically room shape is defined in 2D by the ceiling/floor super-pixels footprint, enforced by the *wall* super-pixels as 2D anchor points. This simplified classification, in absence of other information, is prone to substantial errors, both in terms of labeling accuracy (Fig. 6(a)), and, above all, in positioning the anchor points (Fig. 6(b)).

In our work, instead, we exploit image grouping (Sec. 4) and recovered clutter models (Sec. 5) to enhance images segmentation and labeling. The goal is to use the extra information to more accurately estimate anchor points and to provide additional constraints for the optimization and recovery of room geometry. In this work, this is done by extending the open source pipeline of Pintore et al. [PGP*18], which works with sparse panoramic imagery.

We summarize the boundaries extraction pipeline in the pseudo-code 1, highlighting (in **bold**) our specific contributions with respect to the original approach [PGP*18]. Starting from the super-pixels segmentation of the original images (*createSP*), we project-back the recovered 3D clutter models on the segmented images (Fig. 6(a)), labeling as *clutter* super-pixels where the projection fall (*labelClutterSP*, and assigning to them the depth of the projected model (*clutterDepth*). Only for the remaining super-pixels, we perform background labeling (e.g., *ceiling, floor, wall*) and 3D features infilling, as described by [PGP*18], (*labelBackgroundSP* and *infillBackgroundSP*).

Using the the panorama-set partitioning algorithm introduced in Sec. 4, we assign each cluster of images to a different room. Then, for each room, we transform labeled super-pixels to 3D facets (ceiling and floor) and 2D anchor points (wall and clutter) (Fig. 6(c). See Pintore et al. [PGP*18] for details). Using this projection, we estimate for each room, according to the original pipeline, a first 2D shape (*shape2D*) from ceiling and floor facets (*estimateShape*).

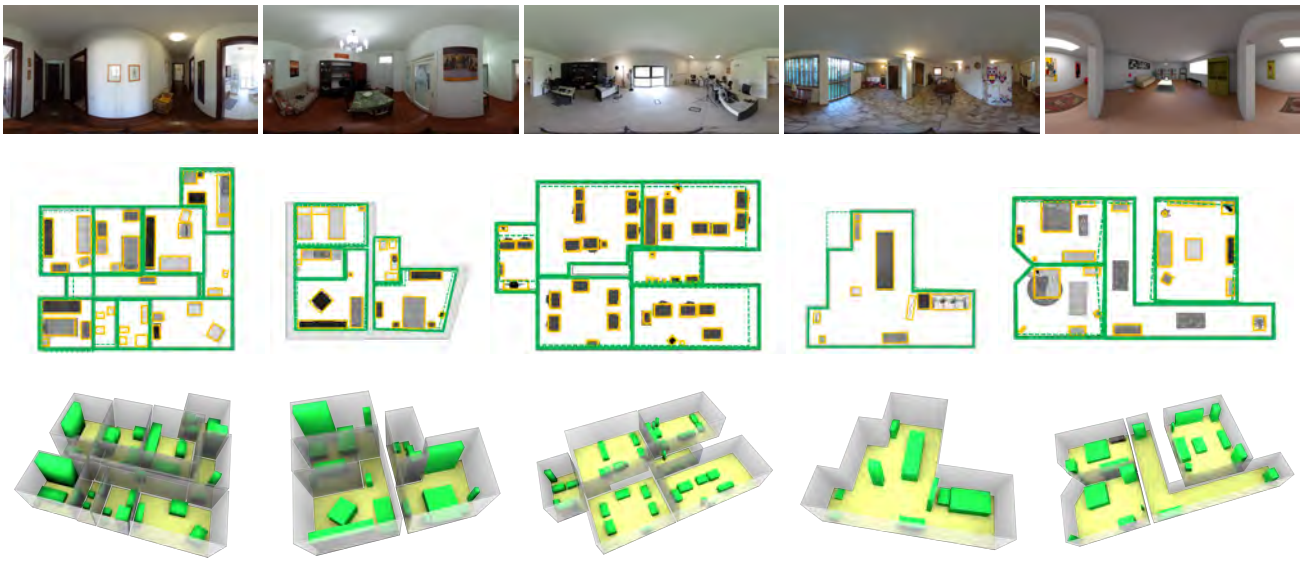

Figure 7: ***Recovered models vs. ground truth.*** *We illustrate, for each dataset, the recovered floorplan models compared vs. ground truth and other approach [PGP*18]. The footprint of recovered objects is illustrated with orange rectangles over the 2D ground truth (e.g., gray background), rooms boundaries reconstructed by our method are showed with green line and rooms boundaries recovered by the other method by dotted green lines. Below the comparison we show 3D views of the recovered models.*

Algorithm 1 Rooms boundaries extraction

I_{eq} equirectangular registered images
F_{3D} multi-view features
C_{3D} clutter models
for all $img \in I_{eq}$ **do**
  $imgSP \leftarrow createSP(img)$
  $maskedSP \leftarrow$ **labelClutterSP**$(imgSP, C_{3D})$
  $labeledSP \leftarrow$ **clutterDepth**$(maskedSP, C_{3D})$
  $labelBackgroundSP(labeledSP)$
  $labeledSP \leftarrow infillBackgroundSP(labeledSP, F_{3D})$
S_{3D} 3D room shapes (empty, to be computed)
$Rooms \leftarrow$ **groupImages**(I_{eq})
for all $r \in Rooms$ **do**
  F_{floor},$F_{ceiling}$ floor and ceiling 3D facets
  A_{wall} wall 2D anchor points
  $A_{clutter}$ clutter 2D anchor points
  $F_{floor}, F_{ceiling} \leftarrow transformToFacets(labeledSP)$
  $A_{wall}, A_{clutter} \leftarrow transformToPoints(labeledSP)$
  filterWallPoints$(A_{wall}, Rooms)$
  $shape2D \leftarrow computeShape(F_{floor}, F_{ceiling})$
  refineShape$(shape2D, A_{wall}, A_{clutter})$
  $shape3D \leftarrow make3D(F_{floor}, F_{ceiling})$
  $S_{3D} \leftarrow shape3D$
buildFloorplan(S_{3D}, C_{3D})

Since the clutter has been explicitly removed, the estimation is much improved in this phase with respect to Pintore et al. [PGP*18], as demonstrated in Sec. 7. We further improve over the original approach (*refineShape*), by pruning wall anchor points using the visibility graph information 4 and by integrating the *clutter* anchor points (Fig. 6(c)) in the shape optimization.

Specifically, we filter-out wall anchor points A_{wall} (*filterWallPoints*) that are seen at the same time by cameras of different visibility groups/rooms (e.g., a typical example of this situation are the points seen through an open door). It should be noted that in our method wall points no longer contain parts of the clutter. Then, we optimize the 2D polygon (*refineShape*) representing the room footprint *shape2D* to not only minimize its distance from wall points A_{wall}, but also imposing that *all* the anchor points $A_{clutter}$ are contained inside the polygon:

$$R_{2k} \equiv \begin{cases} argmin[dist(A_{wall}, shape2D)] \\ \quad \bar{R} \\ shape2D \ni A_{clutter} \end{cases} \tag{4}$$

where each *shape2D* hypothesis is generated by varying a vector of $2k$ corners $\bar{R}(x_0, y_0, \cdots, x_k, y_k)$ [PGP*18], and imposing for each step that $A_{clutter}$ points must be contained inside the candidate shape. Once the 2D walls arrangement is optimized, we extrude the 3D room using floor and ceiling 3D information (*make3D*).

Finally, we join in the same 3D representation the 3D clutter C_{3D} and all the 3D boundaries S_{3D} (*buildFloorplan*). The partitioning data is then used to complete the model with the passages between rooms (i.e., weak arcs on the camera trajectory4), determining whether they are doors or open passages.

7 Results

Our reconstruction pipeline is implemented in C++ on top of *OpenCV*. For multiview alignment we use *Photoscan* `http://www.agisoft.com/`). The system, starting from a collection of spherical images and their multi-view alignment, automatically produces a structured 3D floor plan in terms of interconnected rooms bounded by floor, walls and ceilings, and including the bounding volumes of clutter objects.

Scene			Clutter error				Imgs per room		Imgs assignement		Room 3D IoU		
Name	Objects	mq.	2D Pos.	Orient.	Area	Height[cm]	Our	[PGP*18]	Our	[PGP*18]	Our	[PGP*18]	[YZ16]
Real-data R1	35/36	96	2 ± 5 *cm*	0.2 ± 1.8 *deg*	2 ± 26 %	2 ± 15 *cm*	2.5	2.6	97 %	76 %	89 %	83 %	75 %
Real-data R2	19/20	78	3 ± 21 *cm*	0.7 ± 2.3 *deg*	2 ± 18 %	1 ± 8 *cm*	3	4	100 %	99 %	90 %	82 %	74 %
Real-data R4	43/44	196	2 ± 8 *cm*	0.4 ± 2.1 *deg*	3 ± 1 %	3 ± 2 *cm*	3	6	91 %	72 %	88 %	74 %	70 %
Real-data R5	10/10	55	4 ± 11 *cm*	0.5 ± 1.0 *deg*	2 ± 8 %	2 ± 3 *cm*	2.5	5	100 %	70 %	91 %	84 %	61 %
Synthetic data S1	20/21	188	4 ± 16 *cm*	0.1 ± 1.0 *deg*	3 ± 32 %	1 ± 5 *cm*	2.5	4	100 %	86 %	90 %	72 %	49 %

Table 1: ***Floorplan performance.*** *We present a summary of performances on large, representative floorplans, detailing clutter and rooms structure reconstruction errors. For each dataset we show the ratio of objects recovered, the scene area, the average and maximum error on recovered objects with respect to ground truth. Besides we present the average number of images needed per room, the percentage of correct images assignment and the resulting 3D intersection-over-union ratio (i.e., average of all rooms) with ground truth, compared to the pipeline of Pintore et al. [PGP*18] and, for completeness with the average results of Yang et al. [YZ16] (i.e, averaging score only for rooms where such single-view approach works).*

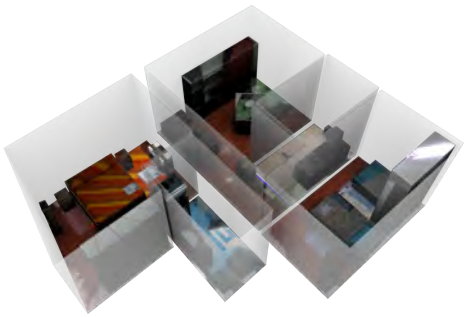

Figure 8: ***Model rendering example.*** *3D rendering of reconstructed R2 dataset with colors from textures.*

	Our		[XSKT17]	
	Pos. Err.	Orient. Err.	Pos. Err.	Orient. Err.
Bed	2 ± 4 *cm*	0.0 ± 1.5 *deg*	25 ± 17 *cm*	1.0 ± 1.4 *deg*
Chair	1 ± 2*cm*	0.5 ± 1.5 *deg*	52 ± 66 *cm*	10.7 ± 15 *deg*
Plant	2 ± 6*cm*	–	9 ± 12 *cm*	–
Overall	3 ± 21*cm*	1.0 ± 3.0 *deg*	28 ± 32 *cm*	4.3 ± 5.7 *deg*

Table 2: ***Object reconstruction comparison.*** *We summarize clutter results for all datasets, detailing performances for some categories, also exposed by the method of Xu et al. [XSKT17]. Our method presents better results in all categories, also taking into account that our results are calculated on a wider variety of rooms. In our approach we also expose orientation error for plants, since, from the space occupation point-of-view, there are a direction of major extension of the canopy (i.e., Fig. 9). .*

7.1 Real and synthetic datasets

We tested the system on a variety of real-world and synthetic scenes, covering over 130 clutter objects of different typologies (bed, cabinet, desk, chair, plant, lamp, lavatory, etc.), belonging to large multi-room environments. To simplify comparisons, we exploited publicly available multi-view data (`http://vic.crs4.it/download/datasets/`), of which measures of rooms and clutter are available. Ground truth objects from real data have been manually modeled, from real laser measures, through representative CAD models having exactly the same size, orientation and position of real clutter, so that they have the same bounding volume of real objects.

In addition, we exploited synthetic datasets to precisely evaluate the system with respect to precise ground-truth data. Specifically, we modeled synthetic scenes by rendering photorealistic equirectangular images of 3D models from another public repository of large indoor scenes (`https://www.ifi.uzh.ch/en/vmml/research/datasets.html`). We have enriched those models with additional clutter and photorealistic details.

For both real and synthetic data, our ground truth model is a metrically scaled (cm) structured 3D floorplan, with floor, ceiling, walls, and major clutter objects inside (i.e., lying on the floor or attached to wall at low heights).

7.2 Reconstruction performance

We run our tests on a PC with Intel Core i7-4770 (3.40GHz) processor and 32GB RAM. Foreground segmentation [YJL*18] takes about 4 *seconds* for each image, meanwhile multi-view registration takes about 2 *minutes* for a dataset of 24 images using *Photoscan*. Object partitioning takes about **10** ***seconds*** for the same dataset of 24 images. Object inference takes about **8** ***seconds*** for each object, as well as boundaries estimation **12** ***seconds*** per room.

7.3 Quantitative evaluation

In Tab. 1, we present quantitative performance in terms of 3D layout recovered, compared to ground truth and with the method of Pintore et al. [PGP*18] and Yang et al. [YZ16] for the boundaries extraction.

We show, for each floor plan, the number of objects actually reconstructed over the number of target objects. We assume as target objects the segmented clutter that is visible from at least two images. The unreconstructed objects are therefore cases of *failure case* of our method, independently by the segmentation performance, which is external to our methods [YJL*18]. Tests demonstrate that our method can fail if object masks do not contain enough geometric cues, as showed,for example, in Fig. 10.

Clutter error shows the average and maximum error on recovered objects with respect to ground truth. We measure positional error (*2D Pos. cm*) as distance between object centroids on the 2D ground plane, orientation error (*Orient. deg*) as the angle between ground truth cuboid and its estimated pose, area error (*Area* percentage %), with respect to ground truth object footprint, and the object height error (*Height cm*). we intentionally separated for the objects the various components (position, area, height), instead of using, for example, intersection-over-union, to facilitate comparison with other clutter modeling methods (Tab. 2).

Our clutter modeling method presents very low average position, orientation and area error in all tests, where the major deviations, especially in term of dimensions, are due mostly to specific cases (e.g., plants, pillows on a bed, TV on a cabinet, etc.) of not well defined shapes. Further details and comparisons on clutter performances are exposed in Tab. 2, Fig.7 and Fig.9.

Imgs per room and *Imgs assignement* show a numerical comparison of our clustering method with a generic geometric approach [PGP*18], which is the most similar to ours, in terms of input data and constraints (see Sec.2). We show how our visual approach allows the entire pipeline to work with a smaller number of images per room, and how, instead, the other approach needs some more images because it discards the images that it is not able to geometrically assign. Moreover our method achieve a better accuracy in the assignment of images (i.e., average compared to all rooms), in particular in the case of semi-open spaces without doors (e.g., *Real-data R4 and R5*).

Room 3D IoU shows instead the 3D intersection-over-union ratio (i.e., average of all room) with ground truth, compared to the pipeline of Pintore et al. [PGP*18], and, for completeness, with the pipeline Yang et al. [YZ16] (`https://github.com/YANG-H/Panoramix`). Yang et al. approach [YZ16], although single-view and limited to simple rooms visible from a single point of view, still offers a term of comparison with these types of approach, since even more recent single view geometric approaches [YJL*18] are based on the same methodology of segmentation and background reconstruction.

In all cases, our approach outperforms the other system, mostly due to the exploitation of image grouping and clutter data fusion in room structure and shape recovery. For the sake of clarity recent data-driven single view methods for room extraction [YWP*19], even if not directly comparable, achieve average 3D IoU performance of about 77% (imposing *Manhattan World* constraint). Fig. 7 illustrates floorplan results, showing the footprint of recovered objects (e.g., orange rectangles) over 2D floorplan (e.g., gray background), rooms boundaries reconstructed by our method (e.g., green line) and rooms boundaries recovered by other method [PGP*18] (e.g., dotted green). In Tab. 2 we summarize clutter results for all datasets,

	Our	[BFFFS14]	[CF14]
Completeness	100%	91%	100%
Accuracy	91%	80%	68%

Table 3: ***Completeness and accuracy comparison.*** *Comparison with other multi-view approaches [BFFFS14, CF14] in terms of the percentage of image pixels whose 3D information can be estimated (*Completeness*), and in terms of percentage of correctly labeled pixels (*Accuracy*).*

detailing performances for some categories, to compare them with the performances of Xu et al. [XSKT17]. Such method for single indoor panoramic images, extends Zhang et al. approach [ZSTX14] to clutter modelling, exposing numerical results comparable with ours (e.g., no numerical results related to the room layout have been made available instead). Our method presents better results in all categories, also taking into account that our results are calculated on a wider variety of rooms, obviously taking advantage of working on more than one view of the same object. In our approach we also expose orientation error for plants, since, from the space occupation point-of-view, there are a direction of major extension of the canopy (i.e., Fig. 9).

In Tab. 3 we show a summary of our performance in terms of the percentage of image pixels whose 3D information can be estimated (*Completeness*), and in terms of percentage of correctly labeled pixels (*Accuracy*). To allow comparison, these values are calculated, by means of synthetic datasets ground truth, on the labeling of individual pixels and not of representative cuboids (Fig. 9(a)). We compare our results with two different multi-view approaches, Bao et al. [BFFFS14] and Cabral and Furukawa [CF14]. As discussed in Sec. 2, Bao et al. [BFFFS14] reconstruct small cluttered indoor scenes (e.g, a room portion), from a set of about 10 pin-hole images. Even if it can be considered, for the number of images required, an almost dense approach, their paper provides numerical results comparable to ours (e.g., code and data are instead not available). It should be note that such method [BFFFS14] recovers only 86% of the objects inside the room, since they cannot recover surfaces that do not contain SFM points. Indeed such value is included in the overall accuracy used for the comparison. Cabral et al. [CF14], instead, adopted equirectangular images to improve indoor reconstruction provided by a dense multi-view pipeline [FCSS09]. Although their full approach is not directly applicable on our sparse data, their super-pixels structure classification can be used as a benchmark, as it provides a complete classification of each individual equirectangular image 9(c) (i.e., source code and data not available, approach implemented according to paper description).

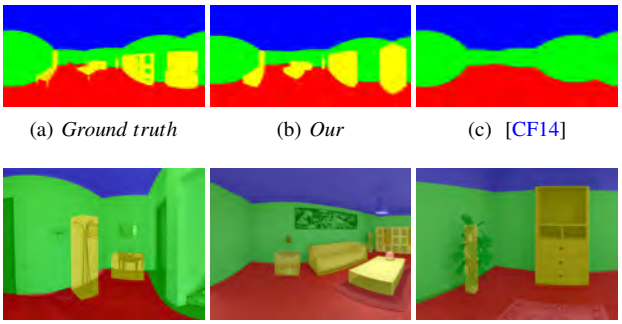

(a) *Ground truth* (b) *Our* (c) [CF14]

(d) *D2 : Coat hanger* (e) *D5 : Round table* (f) *D5 : Plant*

Figure 9: ***Re-projection of recovered models and image labeling.*** *On the first row we present a comparison, on the same example image of* Dataset5*, between ground truth 9(a), our method 9(b) and the semi-dense approach of Cabral et al. 9(c). On the second row we show some example of particular object reconstructed by our method. As the hanger 9(d) and the rounded table 9(e) are correctly represented with their boundaries, approximation of the plant leads to a 2D size error on venge 9(f), although the real footprint size (i.e., plant pot) is correct.*

Results show that our method guarantees a reconstruction of the scene even in the parts without 3D points, and an accuracy higher than compared approaches even if using a limited number of images (Fig.9(b)).

Fig. 10 shows instead examples of failure cases. As described in the previous sections, our method needs at least two segmented views of the object to be reconstructed, which must somehow contain consistent clues of shape and color. Fig. 10(a) shows two image masks of the same object (i.e., a refrigerator), but, due of identical adjacent structures and low saliency in the right view, the masks contain contrasting clues. Since, geometrically, they have a common surface that projects into the same portion of 2D plane (see Sec.5.3), these masks are wrongly matched. In this case, our algorithm is not able to converge to the right solution. Fig. 10(b) shows a case of occlusion affecting the object footprint. Also in this case objects have been recognized and matched, but the first view (e.g., left image) does not contain information about object footprint. we have

(a) *Mask ambiguity* (b) *Occlusion*

Figure 10: ***Example of failure cases.*** *Fig. 10(a) shows two masks of the same object but with contrasting clues. Fig. 10(b) shows instead two masks correctly recognized but with a fatal occlusion in the right one.*

experienced that these cases depend mainly on the position of the image and not on the scene. In particular, images taken too far away from the object or from a not optimal pose are more subject to errors, especially for masks matching.

8 Conclusion

We have presented a light-weight approach to capture and automatically reconstruct structured 3D models of cluttered multi-room floor plans. The method starts from a small set of overlapping panoramic images, which can be very rapidly captured with commodity devices and, as show by our results, is capable to generate automatically a 3D layout of the rooms and of all major objects inside. Such a 3D layout is directly suitable for use in a number of real-world applications, such as guidance, location, routing, or content creation for security.

Our main advantages are in providing a full pipeline that exploits an automatic partitioning into rooms and seamlessly merges clutter detection and room shape reconstruction to quickly produce, in a fully As demonstrated by our results, for similar environments, our approach, in addition to providing shape and location of 3D interior objects, also increases the precision in the recovery of the wall structures with respect to competing methods working on sparse panoramic images.

In our future work, we plan to exploit the reconstructed semantic models for simulation and visualization in the security areas, and to further enrich it with semantic information attached to objects, also going towards automatic 3D modeling by replacing the cuboid approximation with fully 3D models using a data-drive approach.

Acknowledgments. Removed for blind reviewing.

References

[BFFFS14] BAO S. Y., FURLAN A., FEI-FEI L., SAVARESE S.: Understanding the 3D layout of a cluttered room from multiple images. In *Proc. IEEE WACV* (2014), pp. 690–697. 2, 3, 10

[BTS*17] BERGER M., TAGLIASACCHI A., SEVERSKY L. M., ALLIEZ P., GUENNEBAUD G., LEVINE J. A., SHARF A., SILVA C. T.: A survey of surface reconstruction from point clouds. *Comput. Graph. Forum 36*, 1 (2017), 301–329. 1

[CF14] CABRAL R., FURUKAWA Y.: Piecewise planar and compact floorplan reconstruction from images. In *Proc. CVPR* (2014), pp. 628–635. 2, 3, 7, 10

[DBK*13] DEL PERO L., BOWDISH J., KERMGARD B., HARTLEY E., BARNARD K.: Understanding bayesian rooms using composite 3D object models. In *Proc. CVPR* (2013), pp. 153–160. 3

[FCSS09] FURUKAWA Y., CURLESS B., SEITZ S. M., SZELISKI R.: Reconstructing building interiors from images. In *Proc. ICCV* (2009), pp. 80–87. 2, 3, 10

[FMR11] FLINT A., MURRAY D., REID I.: Manhattan scene understanding using monocular, stereo, and 3D features. In *Proc. ICCV* (2011), pp. 2228–2235. 2

[GPMAL09] GOLPARVAR FARD M., PEA-MORA F., ARBOLEDA C., LEE S.: Visualization of construction progress monitoring with 4d simulation model overlaid on time-lapsed photographs. *Journal of Computing in Civil Engineering 23*, 6 (2009), 391–404. 2

[HDGN17] HUANG J., DAI A., GUIBAS L., NIESSNER M.: 3Dlite: Towards commodity 3D scanning for content creation. *ACM TOG 36*, 6 (2017), 203:1–203:14. 2

[HHF10] HEDAU V., HOIEM D., FORSYTH D.: Thinking inside the box: Using appearance models and context based on room geometry. In *Proc. ECCV* (2010), pp. 224–237. 3

[HHF12] HEDAU V., HOIEM D., FORSYTH D.: Recovering free space of indoor scenes from a single image. In *Proc. CVPR* (2012), pp. 2807–2814. 2, 3

[HK01] HAREL D., KOREN Y.: On clustering using random walks. In *Proc. FST TCS* (2001), pp. 18–41. 4

[IYF15] IKEHATA S., YANG H., FURUKAWA Y.: Structured indoor modeling. In *Proc. ICCV* (2015), pp. 1323–1331. 1, 2

[LGHK10] LEE D. C., GUPTA A., HEBERT M., KANADE T.: Estimating spatial layout of rooms using volumetric reasoning about objects and surfaces. In *Proc. NIPS* (2010), pp. 1288–1296. 2, 3

[MMJV*14] MURA C., MATTAUSCH O., JASPE VILLANUEVA A., GOBBETTI E., PAJAROLA R.: Automatic room detection and reconstruction in cluttered indoor environments with complex room layouts. *Computers & Graphics 44* (2014), 20–32. 1

[MMP16] MURA C., MATTAUSCH O., PAJAROLA R.: Piecewise-planar reconstruction of multi-room interiors with arbitrary wall arrangements. *Computer Graphics Forum 35*, 7 (2016), 179–188. 2

[PGGS16] PINTORE G., GANOVELLI F., GOBBETTI E., SCOPIGNO R.: Mobile mapping and visualization of indoor structures to simplify scene understanding and location awareness. In *ECCV Workshops* (2016), pp. 130–145. 2

[PGP*18] PINTORE G., GANOVELLI F., PINTUS R., SCOPIGNO R., GOBBETTI E.: 3D floor plan recovery from overlapping spherical images. *Computational Visual Media 4*, 4 (2018), 367–383. 2, 3, 7, 8, 9, 10

[PPG*18] PINTORE G., PINTUS R., GANOVELLI F., SCOPIGNO R., GOBBETTI E.: Recovering 3D existing-conditions of indoor structures from spherical images. *Computers & Graphics 77* (2018), 16–29. 3

[SCD*06] SEITZ S. M., CURLESS B., DIEBEL J., SCHARSTEIN D., SZELISKI R.: A comparison and evaluation of multi-view stereo reconstruction algorithms. In *Proc. CVPR* (2006), vol. 1, pp. 519–528. 2

[SFPU13] SCHWING A. G., FIDLER S., POLLEFEYS M., URTASUN R.: Box in the box: Joint 3D layout and object reasoning from single images. In *Proc. ICCV* (2013), pp. 353–360. 3

[SQLG15] SU H., QI C. R., LI Y., GUIBAS L. J.: Render for CNN: Viewpoint estimation in images using cnns trained with rendered 3D model views. In *Proc. ICCV* (2015), pp. 2686–2694. 3

[SRLH14] SATKIN S., RASHID M., LIN J., HEBERT M.: 3DNN: 3D nearest neighbor. data-driven geometric scene understanding using 3d models. *International Journal of Computer Vision 111* (2014), 69–97. 3

[TCZ15] TURNER E., CHENG P., ZAKHOR A.: Fast, automated, scalable generation of textured 3d models of indoor environments. *IEEE Journal of Selected Topics in Signal Processing 9*, 3 (2015), 409–421. 1, 2

[TKCM16] TULSIANI S., KAR A., CARREIRA J., MALIK J.: Learning category-specific deformable 3d models for object reconstruction. *IEEE TPAMI 39*, 4 (2016), 719–731. 3

[TXLK11] TSAI G., XU C., LIU J., KUIPERS B.: Real-time indoor scene understanding using bayesian filtering with motion cues. In *Proc. ICCV* (2011), pp. 121–128. 2

[XAAH13] XIONG X., ADAN A., AKINCI B., HUBER D.: Automatic creation of semantically rich 3D building models from laser scanner data. *Automation in Construction 31* (2013), 325–337. 2

[XF14] XIAO J., FURUKAWA Y.: Reconstructing the world's museums. *International Journal of Computer Vision 110*, 3 (Dec 2014), 243–258. 2

[XMS14] XIANG Y., MOTTAGHI R., SAVARESE S.: Beyond PASCAL: A benchmark for 3D object detection in the wild. In *Proc. WACV* (2014), pp. 75–82. 3

[XSKT17] XU J., STENGER B., KEROLA T., TUNG T.: Pano2CAD: Room layout from a single panorama image. In *Proc. WACV* (2017), pp. 354–362. 3, 9, 10

[YJL*18] YANG Y., JIN S., LIU R., , YU J.: Automatic 3D indoor scene modeling from single panorama. In *Proc. CVPR* (2018), pp. 3926–3934. 2, 3, 5, 9, 10

[YWP*19] YANG S.-T., WANG F.-E., PENG C.-H., WONKA P., SUN M., CHU H.-K.: DuLa-Net: A dual-projection network for estimating room layouts from a single RGB panorama. In *Proc. IEEE CVPR* (2019). 3, 10

[YZ16] YANG H., ZHANG H.: Efficient 3D room shape recovery from a single panorama. In *Proc. CVPR* (2016), pp. 5422–5430. 2, 3, 9, 10

[ZCC16] ZHANG E., COHEN M. F., CURLESS B.: Emptying, refurnishing, and relighting indoor spaces. *ACM TOG 35*, 6 (2016), 174:1–174:14. 2

[ZCSH18] ZOU C., COLBURN A., SHAN Q., HOIEM D.: LayoutNet: Reconstructing the 3d room layout from a single rgb image. In *Proc. CVPR* (2018), pp. 2051–2059. 3

[ZSTX14] ZHANG Y., SONG S., TAN P., XIAO J.: Panocontext: A whole-room 3d context model for panoramic scene understanding. In *Proc. ECCV* (2014), pp. 668–686. 2, 3, 10